Obtaining the complex pressure field at the hologram surface for use in near-field acoustical holography when pressure and in-plane velocities are measured

Michael C. Harris and Jonathan D. Blotter[a]
Department of Mechanical Engineering, Brigham Young University, 435 CTB, Provo, Utah 84602

Scott D. Sommerfeldt
Department of Physics and Astronomy, Brigham Young University, N281A ESC, Provo, Utah 84602

(Received 12 April 2005; revised 31 October 2005; accepted 28 November 2005)

Acoustical-based imaging techniques have found merit in determining the behavior of vibrating structures. These techniques are commonly used in numerous applications to obtain detailed noise source information and energy distributions on source surfaces. Source reconstructions using near-field acoustical holography (NAH) are reliant upon accurate measurement of the pressure field at the hologram surface. For complex acoustic fields this requires fine spatial resolution and therefore demands large microphone arrays. In this paper, an interpolation method is developed for obtaining the complex pressure field at the hologram surface from pressure and velocity measurements. Because particle velocity measurements provide directional information, a more accurate characterization of the pressure field with fewer measurement locations is obtained. The processing technique presented does not relate directly to the holographic reconstruction itself. However, the interpolation scheme presented serves as a preprocessing step before a NAH algorithm is applied. The presentation and validation of the interpolation scheme is the major focus of the paper. An analytical comparison of NAH reconstructions from traditional pressure measurements to reconstructions using the preprocessed pressure and velocity measurements is presented. A vibrating plate and cylinder are considered as test cases to validate the analytical results. © *2006 Acoustical Society of America.* [DOI: 10.1121/1.2159427]

PACS number(s): 43.20.Ye, 43.40.At, 43.60.Pt [EGW] Pages: 808–816

I. INTRODUCTION

Near-field acoustic holography (NAH) is a methodology that enables the reconstruction of acoustic quantities in three-dimensional space from a two-dimensional measurement of the pressure field near the surface. Williams and Maynard presented a Fourier transform-based NAH method[1–3] for separable geometries of the wave equation that has been successfully applied to a variety of radiation problems.[4–6] Two approaches are currently available for arbitrary geometry problems. The first technique solves the Helmholtz integral equation numerically via the inverse boundary element method (IBEM).[7,8] An alternative to IBEM is the Helmholtz equation least-squares (HELS)[9,10] method which reconstructs the acoustic field using spherical basis functions.

One common aspect of all three NAH implementations is that the accuracy of reconstruction is dependent upon adequate representation of the pressure field on the measurement surface. The Fourier transform method and the IBEM rely on a spatial sampling for field characterization, which can cause mid- to high-frequency measurements to become cumbersome. This is due to the fact that the microphone spacing must be less than or equal to a half wavelength of the highest frequency of interest to avoid spatial aliasing.

The objective of this work is to develop a processing technique for pressure and velocity measurements that provides an improved characterization of the pressure field at the hologram surface. The result would be a reduction in the number of required measurement locations. This would lead to a considerable savings in data acquisition time for scanning array systems and help reduce the inefficiencies encountered at high frequencies.

Acoustic pressure and quadratic pressure measurements were used for NAH by Loyau *et al.*[11] in their development of broadband acoustic holography from intensity measurements (BAHIM) to obtain the phase of the pressure hologram without the need of a reference for scanning array systems. Visser[12] also showed that a particle velocity based adaptive boundary element method performs better than the conventional pressure based implementation if the pressure and velocity measurements have comparable signal-to-noise ratios.

This work relies on the ability to accurately measure acoustic particle velocity. Presently, the primary technique for particle velocity estimation is via finite difference approximations. The accuracy of this method depends on error in the pressure difference, scattering and diffraction, and microphone phase mismatch. Recently, a new particle velocity transducer known as a Microflown[13] sensor has been developed which functions similar to a hot wire anemometer. The transducer consists of two thin, parallel wires five microns apart that are heated to approximately 300 °C. As air particles flow across the wires heat transfer occurs. The first wire crossed will heat the air slightly which results in the second wire not being cooled to quite the same degree. This

---

[a] Electronic mail: jblotter@byu.edu

temperature difference is then used to determine the particle velocity. Jacobsen and de Bree[14] showed that results comparable to finite difference intensity approximations are possible using the Microflown to measure the particle velocity. For the work presented in this paper, the Microflown sensor is used. However, the results are applicable to any sensor that measures both pressure and particle velocity, such as the energy density probe discussed in Ref. 15.

This paper presents a method where near-field pressure and in-plane velocities are used to obtain a representation of the pressure field at the measurement contour. The pressure and velocity field information are combined using a modified bicubic Hermite interpolation scheme presented in Sec. II. The work presented in this paper does not modify the currently used NAH algorithms discussed earlier. It does, however, provide the user with a better characterization of the field on the measurement surface to input into one of the currently available NAH algorithms. Analytical results are presented to indicate the theoretical benefits of the proposed preprocessing method. Experimental results for planar and cylindrical test cases are included for model validation. Because separable geometries have been chosen, the Fourier transform-based NAH method is implemented. However, the interpolation method presented in the following is applicable to arbitrary geometry problems if the IBEM or HELS method is selected.

II. PRESSURE FIELD INTERPOLATION THEORY

Current NAH reconstruction methods are based solely on measurement of the pressure field. Since pressure is a scalar quantity, it does not provide directional information for the field. Particle velocity measurements, on the other hand, supply first derivative information for the pressure field via Euler's equation,

$$\rho_0 \frac{\partial \vec{u}}{\partial t} = -\nabla p. \tag{1}$$

The measured in-plane velocities make derivative information available that is used to interpolate between measurement locations. This effectively simulates a finer mesh of pressure measurements.

Hermite Interpolation. The chosen interpolation method is taken from the area of geometric modeling.[16] For ease of programming and computability, along with other reasons specific to geometric modeling, the preferred way to perform interpolation is with parametric equations. For example, a three-dimensional curve is defined by $x = x(r,s), y = y(r,s)$, and $z = z(r,s)$. It is generally convenient to normalize the domain of the parametric variables, r and s, by restricting their values to the closed interval between 0 and 1, inclusive. This restriction is expressed symbolically as $r,s \in [0,1]$. This interval establishes the bounding curves and the intermediate interpolation points. These curves have a natural vector representation given by

$$\mathbf{f}(r,s) = [x(r,s)\ y(r,s)\ z(r,s)]. \tag{2}$$

Farin[17] points out that a piecewise lower order polynomial interpolation approach is superior in speed and accuracy to its higher order counterparts. Therefore, bicubic polynomial interpolation is selected. Hermite surface patches are chosen for interpolation between measurement locations because they match both function values and slopes at the specified corner points.

Curves. Bicubic Hermite surfaces are composed of an orthogonal net of cubic Hermite curves. Therefore, a preliminary discussion of these curves is necessary to provide the foundation upon which the surface interpolation is built. For a more detailed development of Hermite interpolation see Ref. 16. The algebraic form of a parametric cubic curve is given by the polynomials in the following:

$$\begin{aligned} x(r) &= a_x r^3 + b_x r^2 + c_x r + d_x, \\ y(r) &= a_y r^3 + b_y r^2 + c_y r + d_y, \\ z(r) &= a_z r^3 + b_z r^2 + c_z r + d_z. \end{aligned} \tag{3}$$

The 12 scalar coefficients, called algebraic coefficients, determine a unique curve. Using vector notation to obtain a more compact form, Eq. (3) becomes

$$\mathbf{f}(r) = \mathbf{a}r^3 + \mathbf{b}r^2 + \mathbf{c}r + \mathbf{d}, \tag{4}$$

where $\mathbf{f}(r)$ is the position vector of any point on the curve and $\mathbf{a}, \mathbf{b}, \mathbf{c}$, and $\mathbf{d}$ are the vector equivalents of the scalar algebraic coefficients. The algebraic coefficients are not the most convenient way of controlling the shape of a curve, nor do they provide an intuitive sense of the curve shape. Converting to the Hermite form allows for the definition of conditions at the curve boundaries, or end points. Using the end points $\mathbf{f}(0)$ and $\mathbf{f}(1)$, the corresponding tangent vectors $\mathbf{f}^r(0)$ and $\mathbf{f}^r(1)$, and Eq. (4) yields the

$$\begin{aligned} \mathbf{f}(0) &= \mathbf{d}, \\ \mathbf{f}(1) &= \mathbf{a} + \mathbf{b} + \mathbf{c} + \mathbf{d}, \\ \mathbf{f}^r(0) &= \mathbf{c}, \\ \mathbf{f}^r(1) &= 3\mathbf{a} + 2\mathbf{b} + \mathbf{c}, \end{aligned} \tag{5}$$

where substituting $r=0$ into Eq. (4) yields $\mathbf{f}(0)$, and substituting $r=1$ into the equation yields $\mathbf{f}(1)$. Differentiating $\mathbf{f}(r)$ with respect to r obtains $\mathbf{f}^r(r) = 3\mathbf{a}r^2 + 2\mathbf{b}r + \mathbf{c}$. Substituting $r=0$ and $r=1$ into this yields $\mathbf{f}^r(0)$ and $\mathbf{f}^r(1)$, respectively, where the superscript r indicates the derivative with respect to r. Solving this set of four simultaneous vector equations in four unknown vectors yields the algebraic coefficients in terms of the boundary conditions,

$$\begin{aligned} \mathbf{a} &= 2\mathbf{f}(0) - 2\mathbf{f}(1) + \mathbf{f}^r(0) + \mathbf{f}^r(1), \\ \mathbf{b} &= -3\mathbf{f}(0) + 3\mathbf{f}(1) - 2\mathbf{f}^r(0) - \mathbf{f}^r(1), \\ \mathbf{c} &= \mathbf{f}^r(0), \\ \mathbf{d} &= \mathbf{f}(0). \end{aligned} \tag{6}$$

Substituting these equations for the algebraic coefficient vectors into Eq. (4) and rearranging terms produces

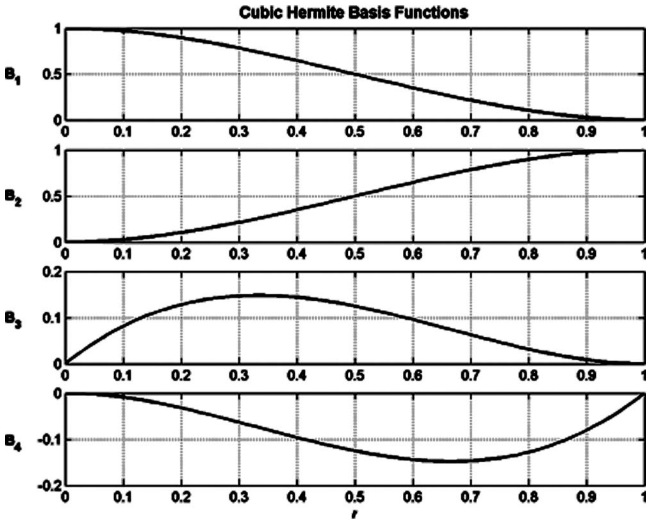

FIG. 1. Plot of the cubic Hermite basis functions in parameter space.

$$\mathbf{f}(r) = (2r^3 - 3r^2 + 1)\mathbf{f}(0) + (-2r^3 + 3r^2)\mathbf{f}(1) + (r^3 - 2r^2 + r)\mathbf{f}^r(0) + (r^3 - r^2)\mathbf{f}^r(1). \tag{7}$$

This equation is simplified by making the following substitutions:

$$\begin{aligned} \mathbf{B}_1(r) &= 2r^3 - 3r^2 + 1, \\ \mathbf{B}_2(r) &= -2r^3 + 3r^2, \\ \mathbf{B}_3(r) &= r^3 - 2r^2 + r, \\ \mathbf{B}_4(r) &= r^3 - r^2. \end{aligned} \tag{8}$$

Using these simplifications and subscripts to represent the end point r values, Eq. (7) becomes

$$\mathbf{f}(r) = \mathbf{B}_1(r)\mathbf{f}_0 + \mathbf{B}_2(r)\mathbf{f}_1 + \mathbf{B}_3(r)\mathbf{f}_0^r + \mathbf{B}_4(r)\mathbf{f}_1^r. \tag{9}$$

Equation (9) is called the geometric form, and the vectors $\mathbf{f}_0, \mathbf{f}_1, \mathbf{f}_0^r$, and $\mathbf{f}_1^r$ are the geometric coefficients. The $\mathbf{B}_i(r)$ terms are called the Hermite basis functions. Figure 1 shows each basis function as a curve over the domain of the parameter r. These basis functions have three important characteristics. First, they are universal for all cubic Hermite curves. Second, they are only dependent on the parameter, making them identical for each of the three real space coordinates. Finally, they allow the constituent boundary condition coefficients to be decoupled from each other. These functions blend the effects of the end points and tangent vectors to produce the intermediate point coordinate values over the parameter domain. Letting

$$\mathbf{R} = [r^3 \quad r^2 \quad r \quad 1],$$

$$\mathbf{M}_H = \begin{bmatrix} 2 & -2 & 1 & 1 \\ -3 & 3 & -2 & -1 \\ 0 & 0 & 1 & 0 \\ 1 & 0 & 0 & 0 \end{bmatrix}, \tag{10}$$

$$\mathbf{G}_H = [\mathbf{f}_0 \quad \mathbf{f}_1 \quad \mathbf{f}_0^r \quad \mathbf{f}_1^r]^T,$$

the geometric form given in Eq. (9) can be transformed into the more computationally efficient matrix form, where $\mathbf{M}_H$ is the Hermite basis transformation matrix and $\mathbf{G}_H$ is the geometry matrix containing the curve boundary conditions,

$$\mathbf{f}(r) = \mathbf{R}\mathbf{M}_H\mathbf{G}_H. \tag{11}$$

The geometry matrix in Eq. (11) is altered for each segment to obtain a series of cubic Hermite curves which are combined to form a composite curve with slope continuity at the end points.

Surfaces. A large complex surface can be defined by a composite collection of simpler patches. The algebraic form of a bicubic Hermite patch is given by the tensor product shown in the following:

$$\mathbf{f}(r,s) = \sum_{i=0}^{3} \sum_{j=0}^{3} \mathbf{a}_{ij} r^i s^j. \tag{12}$$

The $\mathbf{a}_{ij}$ are the three component algebraic coefficient vectors of the patch, where each component represents one of the three dimensions in real space. The subscripting corresponds to the order of the parameter variables that the coefficient is attributed to. Expanding Eq. (12) and arranging the $\mathbf{a}_{ij}$ terms in descending order produces Eq. (13), a 16 term polynomial in r and s,

$$\begin{aligned} \mathbf{f}(r,s) = {} & \mathbf{a}_{33}r^3s^3 + \mathbf{a}_{32}r^3s^2 + \mathbf{a}_{31}r^3s + \mathbf{a}_{30}r^3 + \mathbf{a}_{23}r^2s^3 \\ & + \mathbf{a}_{22}r^2s^2 + \mathbf{a}_{21}r^2s + \mathbf{a}_{20}r^2 + \mathbf{a}_{13}rs^3 + \mathbf{a}_{12}rs^2 \\ & + \mathbf{a}_{11}rs + \mathbf{a}_{10}r + \mathbf{a}_{03}s^3 + \mathbf{a}_{02}s^2 + \mathbf{a}_{01}s + \mathbf{a}_{00}. \end{aligned} \tag{13}$$

Because each of the 16 vector coefficients $\mathbf{a}_{ij}$ has three independent components, there are a total of 48 algebraic coefficients, or 48 degrees of freedom. In matrix notation, the algebraic form is

$$\mathbf{f}(r,s) = \mathbf{R}\mathbf{A}\mathbf{S}^T, \tag{14}$$

where

$$\begin{aligned} \mathbf{R} &= [r^3 \quad r^2 \quad r \quad 1], \\ \mathbf{S} &= [s^3 \quad s^2 \quad s \quad 1], \\ \mathbf{A} &= \begin{bmatrix} \mathbf{a}_{33} & \mathbf{a}_{32} & \mathbf{a}_{31} & \mathbf{a}_{30} \\ \mathbf{a}_{23} & \mathbf{a}_{22} & \mathbf{a}_{21} & \mathbf{a}_{20} \\ \mathbf{a}_{13} & \mathbf{a}_{12} & \mathbf{a}_{11} & \mathbf{a}_{10} \\ \mathbf{a}_{03} & \mathbf{a}_{02} & \mathbf{a}_{01} & \mathbf{a}_{00} \end{bmatrix}. \end{aligned} \tag{15}$$

Since the $\mathbf{a}$ elements are three-component vectors, the $\mathbf{A}$ matrix is actually a $4 \times 4 \times 3$ array. As was found with Hermite curves, the algebraic coefficients of a Hermite patch determine its shape and position in space. Although the r,s parameter domain values are restricted between 0 and 1, the range of the variables in x, y, and z is not restricted, because the range of the algebraic coefficients is not limited. A unique point on the surface patch is generated each time a specific pair of r,s values are input into Eq. (14). These pairs of r,s values are then mapped back into real space.

Each patch is bounded by four curves, and each boundary curve is a cubic Hermite curve. Applying the same subscripting notation as implemented in Eq. (9), these curves are denoted as: $\mathbf{f}_{0s}, \mathbf{f}_{1s}, \mathbf{f}_{r0}$, and $\mathbf{f}_{r1}$, because they arise at the limit values of the parametric variables. There are also four unique corner points $\mathbf{f}_{00}, \mathbf{f}_{01}, \mathbf{f}_{10}$, and $\mathbf{f}_{11}$. As was seen for curves, the geometric form is a more convenient and intuitive way to define a patch. The geometric form is derived in the same way as for curves. The boundary conditions of the patch are used to solve for the algebraic coefficients. These conditions include the four patch corner points $\mathbf{f}_{00}, \mathbf{f}_{01}, \mathbf{f}_{10}, \mathbf{f}_{11}$ and the eight tangent vectors $\mathbf{f}^{r}_{00}, \mathbf{f}^{s}_{00}, \mathbf{f}^{r}_{10}, \mathbf{f}^{s}_{10}, \mathbf{f}^{r}_{01}, \mathbf{f}^{s}_{01}, \mathbf{f}^{r}_{11}, \mathbf{f}^{s}_{11}$ which define the boundary curves. $\mathbf{B}$ once again represents the Hermite basis functions, as in Eq. (9),

$$
\begin{aligned}
\mathbf{f}(r,0) &= \mathbf{B}(r)[\mathbf{f}_{00} \quad \mathbf{f}_{10} \quad \mathbf{f}^{r}_{00} \quad \mathbf{f}^{r}_{10}]^{T},\\
\mathbf{f}(r,1) &= \mathbf{B}(r)[\mathbf{f}_{01} \quad \mathbf{f}_{11} \quad \mathbf{f}^{r}_{01} \quad \mathbf{f}^{r}_{11}]^{T},\\
\mathbf{f}(0,s) &= \mathbf{B}(s)[\mathbf{f}_{00} \quad \mathbf{f}_{01} \quad \mathbf{f}^{s}_{00} \quad \mathbf{f}^{s}_{01}]^{T},\\
\mathbf{f}(1,s) &= \mathbf{B}(s)[\mathbf{f}_{10} \quad \mathbf{f}_{11} \quad \mathbf{f}^{s}_{10} \quad \mathbf{f}^{s}_{11}]^{T}.
\end{aligned}
\tag{16}
$$

These four curves provide 12 of the 16 vectors needed to specify the 48 degrees of freedom. Four additional vectors at the corner points, called twist vectors, are used to fully specify the patch. Mathematically, these vectors are defined as follows:

$$
\begin{aligned}
\mathbf{f}^{rs}_{00} &= \frac{\partial^2 \mathbf{f}(r,s)}{\partial r\,\partial s} \quad \text{at } r=0, s=0,\\
\mathbf{f}^{rs}_{10} &= \frac{\partial^2 \mathbf{f}(r,s)}{\partial r\,\partial s} \quad \text{at } r=1, s=0,\\
\mathbf{f}^{rs}_{01} &= \frac{\partial^2 \mathbf{f}(r,s)}{\partial r\,\partial s} \quad \text{at } r=0, s=1,\\
\mathbf{f}^{rs}_{11} &= \frac{\partial^2 \mathbf{f}(r,s)}{\partial r\,\partial s} \quad \text{at } r=1, s=1.
\end{aligned}
\tag{17}
$$

Calculating the mixed partial derivative of Eq. (13) yields

$$
\begin{aligned}
\frac{\partial^2 \mathbf{f}(r,s)}{\partial r\,\partial s} &= 9\mathbf{a}_{33}r^2s^2 + 6\mathbf{a}_{32}r^2s + 3\mathbf{a}_{31}r^2 + 6\mathbf{a}_{23}rs^2 + 4\mathbf{a}_{22}rs\\
&\quad + 2\mathbf{a}_{21}r + 3\mathbf{a}_{13}s^2 + 2\mathbf{a}_{12}s + \mathbf{a}_{11}.
\end{aligned}
\tag{18}
$$

Evaluating Eq. (18) at the corner points obtains

$$
\begin{aligned}
\mathbf{f}^{rs}_{00} &= \mathbf{a}_{11},\\
\mathbf{f}^{rs}_{10} &= 3\mathbf{a}_{31} + 2\mathbf{a}_{21} + \mathbf{a}_{11},\\
\mathbf{f}^{rs}_{01} &= 3\mathbf{a}_{13} + 2\mathbf{a}_{12} + \mathbf{a}_{11},\\
\mathbf{f}^{rs}_{11} &= 9\mathbf{a}_{33} + 6\mathbf{a}_{32} + 3\mathbf{a}_{31} + 6\mathbf{a}_{23} + 4\mathbf{a}_{22} + 2\mathbf{a}_{21} + 3\mathbf{a}_{13}\\
&\quad + 2\mathbf{a}_{12} + \mathbf{a}_{11}.
\end{aligned}
\tag{19}
$$

Doing the same for the remaining 12 vectors provides the remaining 12 equations required to solve for the algebraic coefficients,

$$
\begin{aligned}
\mathbf{f}_{00} &= \mathbf{a}_{00},\\
\mathbf{f}_{10} &= \mathbf{a}_{30} + \mathbf{a}_{20} + \mathbf{a}_{10} + \mathbf{a}_{00},\\
\mathbf{f}_{01} &= \mathbf{a}_{03} + \mathbf{a}_{02} + \mathbf{a}_{01} + \mathbf{a}_{00},\\
\mathbf{f}_{11} &= \mathbf{a}_{33} + \mathbf{a}_{32} + \mathbf{a}_{31} + \mathbf{a}_{30} + \mathbf{a}_{23} + \mathbf{a}_{22} + \mathbf{a}_{21} + \mathbf{a}_{20} + \mathbf{a}_{13}\\
&\quad + \mathbf{a}_{12} + \mathbf{a}_{11} + \mathbf{a}_{10} + \mathbf{a}_{03} + \mathbf{a}_{02} + \mathbf{a}_{01} + \mathbf{a}_{00},\\
\mathbf{f}^{r}_{00} &= \mathbf{a}_{10},\\
\mathbf{f}^{s}_{00} &= \mathbf{a}_{01},\\
\mathbf{f}^{r}_{10} &= 3\mathbf{a}_{30} + 2\mathbf{a}_{20} + \mathbf{a}_{10},\\
\mathbf{f}^{s}_{10} &= \mathbf{a}_{31} + \mathbf{a}_{21} + \mathbf{a}_{11} + \mathbf{a}_{01},\\
\mathbf{f}^{r}_{01} &= \mathbf{a}_{13} + \mathbf{a}_{12} + \mathbf{a}_{11} + \mathbf{a}_{10},\\
\mathbf{f}^{s}_{01} &= 3\mathbf{a}_{03} + 2\mathbf{a}_{02} + \mathbf{a}_{01},\\
\mathbf{f}^{r}_{11} &= 3\mathbf{a}_{33} + 3\mathbf{a}_{32} + 3\mathbf{a}_{31} + \mathbf{a}_{30} + 2\mathbf{a}_{23} + 2\mathbf{a}_{22} + 2\mathbf{a}_{21} + 2\mathbf{a}_{20}\\
&\quad + \mathbf{a}_{13} + \mathbf{a}_{12} + \mathbf{a}_{11} + \mathbf{a}_{10},\\
\mathbf{f}^{s}_{11} &= 3\mathbf{a}_{33} + 2\mathbf{a}_{32} + \mathbf{a}_{31} + 3\mathbf{a}_{23} + 2\mathbf{a}_{22} + \mathbf{a}_{21} + 3\mathbf{a}_{13} + 2\mathbf{a}_{12}\\
&\quad + \mathbf{a}_{11} + 3\mathbf{a}_{03} + 2\mathbf{a}_{02} + \mathbf{a}_{01}.
\end{aligned}
\tag{20}
$$

Solving this set of 16 simultaneous equations from Eqs. (19) and (20) for the algebraic coefficients in terms of the geometric inputs and rearranging terms yields

$$
\begin{aligned}
\mathbf{f}(r,s) &= [\mathbf{B}_1(r) \quad \mathbf{B}_2(r) \quad \mathbf{B}_3(r) \quad \mathbf{B}_4(r)]\mathbf{G}_H\\
&\quad \times [\mathbf{B}_1(s) \quad \mathbf{B}_2(s) \quad \mathbf{B}_3(s) \quad \mathbf{B}_4(s)]^{T},
\end{aligned}
\tag{21}
$$

where $\mathbf{G}_H$ is the Hermite geometry matrix shown in the following:

$$
\mathbf{G}_H = \begin{bmatrix}
\mathbf{f}_{00} & \mathbf{f}_{01} & \mathbf{f}^{s}_{00} & \mathbf{f}^{s}_{01}\\
\mathbf{f}_{10} & \mathbf{f}_{11} & \mathbf{f}^{s}_{10} & \mathbf{f}^{s}_{11}\\
\mathbf{f}^{r}_{00} & \mathbf{f}^{r}_{01} & \mathbf{f}^{rs}_{00} & \mathbf{f}^{rs}_{01}\\
\mathbf{f}^{r}_{10} & \mathbf{f}^{r}_{11} & \mathbf{f}^{rs}_{10} & \mathbf{f}^{rs}_{11}
\end{bmatrix}.
\tag{22}
$$

Recalling from Eq. (11) that $\mathbf{B}(r)$ may be expressed as $\mathbf{RM}_H$, Eq. (21) may be further simplified to obtain the conventional geometric form given by

$$
\mathbf{f}(r,s) = \mathbf{RM}_H\mathbf{G}_H\mathbf{M}_H\mathbf{S}^{T}.
\tag{23}
$$

The remaining intricacy of the interpolation relates to converting between real and parameter space. A simple method for mapping between the two domains is presented in the following. Figure 2 provides an example of a set of four corner points in x and y that could be used to define a patch. In this case, the r parameter corresponds to the x direction and the s parameter to the y direction. Each (x,y)

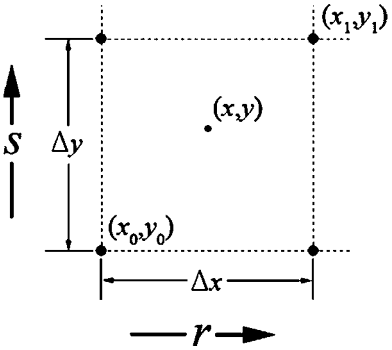

FIG. 2. Four corner points that could be used to define a Hermite surface patch.

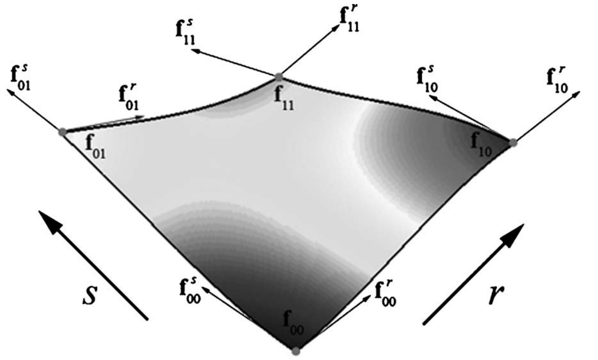

FIG. 3. A sample bicubic Hermite surface patch showing the required inputs at each corner point.

coordinate pair inside the patch corresponds to an (r,s) parameter pair. This parameter pair is obtained using

$$r=\frac{x-x_0}{\Delta x},\qquad s=\frac{y-y_0}{\Delta y}, \tag{24}$$

where Δx and Δy correspond to the spacing between corner points in x and y, respectively. The slopes at the end points must also be transformed to the parameter domain. This is accomplished by scaling the r derivatives by Δx and the s derivatives by Δy as shown in Eq. (25) for the corner point corresponding to $r=s=0$,

$$\mathbf{f}^r_{00}=\frac{\partial \mathbf{f}_{00}}{\partial x}\cdot\frac{\Delta x}{\Delta r},\qquad \mathbf{f}^s_{00}=\frac{\partial \mathbf{f}_{00}}{\partial y}\cdot\frac{\Delta y}{\Delta s}, \tag{25}$$

where Δr and Δs equal one because they are restricted to vary from zero to one. The form is the same for the remaining three corner points of the patch.

Because measurements with pressure and velocity sensors do not in general provide enough information to calculate twist vectors, they have been set to zero for this investigation. The Hermite geometry matrix from Eq. (22) then becomes

$$\mathbf{G}_H=\begin{bmatrix}\mathbf{f}_{00} & \mathbf{f}_{01} & \mathbf{f}^s_{00} & \mathbf{f}^s_{01}\\ \mathbf{f}_{10} & \mathbf{f}_{11} & \mathbf{f}^s_{10} & \mathbf{f}^s_{11}\\ \mathbf{f}^r_{00} & \mathbf{f}^r_{01} & 0 & 0\\ \mathbf{f}^r_{10} & \mathbf{f}^r_{11} & 0 & 0\end{bmatrix}. \tag{26}$$

This limits the patches to having only first derivative continuity at their edges. The results presented in the following indicate that adequate reconstructions are still obtained with this simplification. A second order fit could also provide first derivative continuity but lacks the ability to interpolate more than a half of a wavelength between measurements. Figure 3 shows a sample bicubic Hermite patch and the required inputs at each corner point $\mathbf{f}_{rs}$. Each patch represents the rectangular area between four corner point locations. The above-noted interpolation is repeated for each segment of the surface and all the patches combined.

III. ANALYTICAL IMPLEMENTATION

With the surface interpolation completed, the chosen NAH algorithm is applied. In this section an analytical model is developed to investigate the theoretical benefits of the pressure field preprocessing method. This model requires first that a synthetic acoustic field be created from a hypothetical source. The field is then sampled and the chosen algorithm implemented. The error is then evaluated on the estimation plane by comparing the actual and reconstructed fields.

A. Synthetic field creation

A rectangular, simply supported plate is chosen as the hypothetical source because it has a simple closed-form radiation equation. The plate shown in Fig. 4 is driven by a

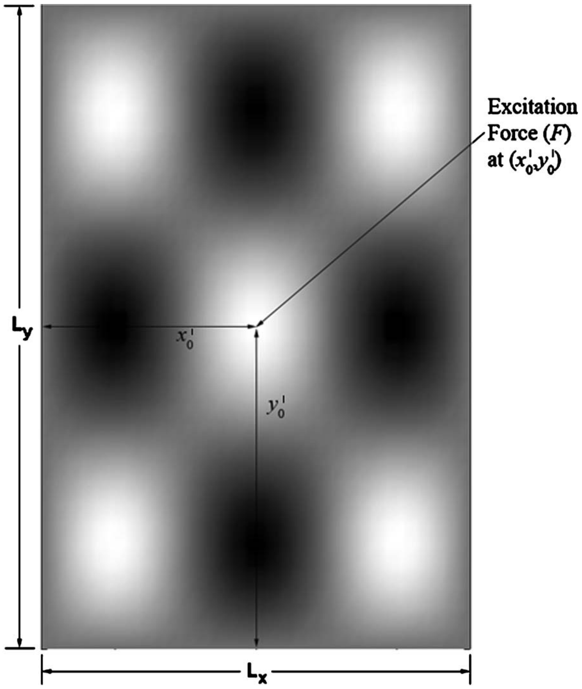

FIG. 4. Geometry of the simply supported plate chosen to be the source for the analytical modeling.

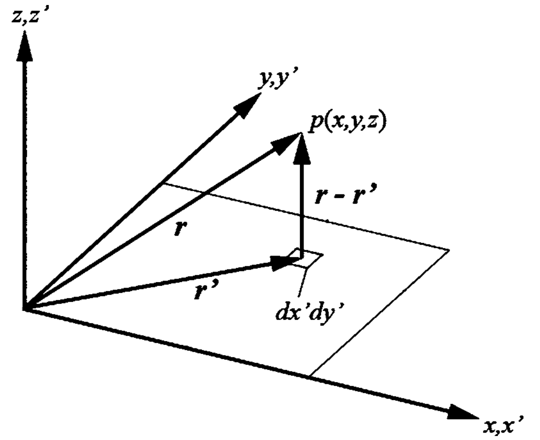

FIG. 5. Description of the geometric quantities used in Rayleigh's integral.

harmonic point source acting normal to the plate at its center (x_0', y_0'). The surface displacement w for the plate as a function of angular frequency ω is given by Eq. (27),[3]

$$w(x', y', \omega) = -\frac{F}{\rho h}\sum_{m=1}^{\infty}\sum_{n=1}^{\infty}\frac{\Phi_{mn}(x_0', y_0')\Phi_{mn}(x', y')}{\omega^2 - \omega_{mn}^2}, \qquad (27)$$

$$\Phi_{mn}(x', y') = \frac{2}{\sqrt{L_x L_y}}\sin\left(\frac{m\pi x'}{L_x}\right)\sin\left(\frac{n\pi y'}{L_y}\right), \qquad (28)$$

where F is the excitation force amplitude, ρ the plate material density per unit area, h the plate thickness, and L the length of the plate in the indicated direction. The subscripts m and n denote the plate mode numbers in the x and y directions, respectively. Assuming that the plate is in an infinite rigid baffle, the radiated pressure can be expressed in terms of the plate surface displacement using Rayleigh's integral. Figure 5 provides a clear description of the geometric quantities to be used in Eq. (29), where $e^{-i\omega t}$ time dependence has been assumed,

$$p(x, y, z, \omega) = -\frac{\omega^2 \rho_0}{2\pi}\int_{-\infty}^{\infty}\int_{-\infty}^{\infty} w(x', y', \omega)\frac{e^{ik|\vec{r}-\vec{r}'|}}{|\vec{r}-\vec{r}'|}dx'dy'. \qquad (29)$$

The pressure at a point in space, $p(x, y, z, \omega)$ is computed by summing the contribution from each $dx'dy'$ area element. Radiation from the plate is simulated using a discrete summation of Eq. (29) for a 32×32 grid of point sources on the plate. The field is then sampled at chosen measurement locations to obtain the pressure and gradient information to be used for interpolation. The selected NAH algorithm is then applied to reconstruct the field.

B. Error evaluation

The reconstruction error is evaluated by first calculating the pressure field at the measurement and estimation planes directly using Eq. (29). The direct calculation of the pressure field at the estimation plane serves as a reference against which the NAH reconstruction is compared. The reconstruction error is quantified by differencing the NAH estimation and the direct calculation at the estimation plane. The standard deviation of these residuals is then computed and normalized by the maximum pressure field value to obtain a single value representing the whole field error. The error for the reconstructions using the preprocessed data is compared to pressure only reconstructions. The number of sensors used to populate the measurement array is varied in both dimensions in order to determine the possible reduction in sensor count using the pressure and in-plane velocity measurements.

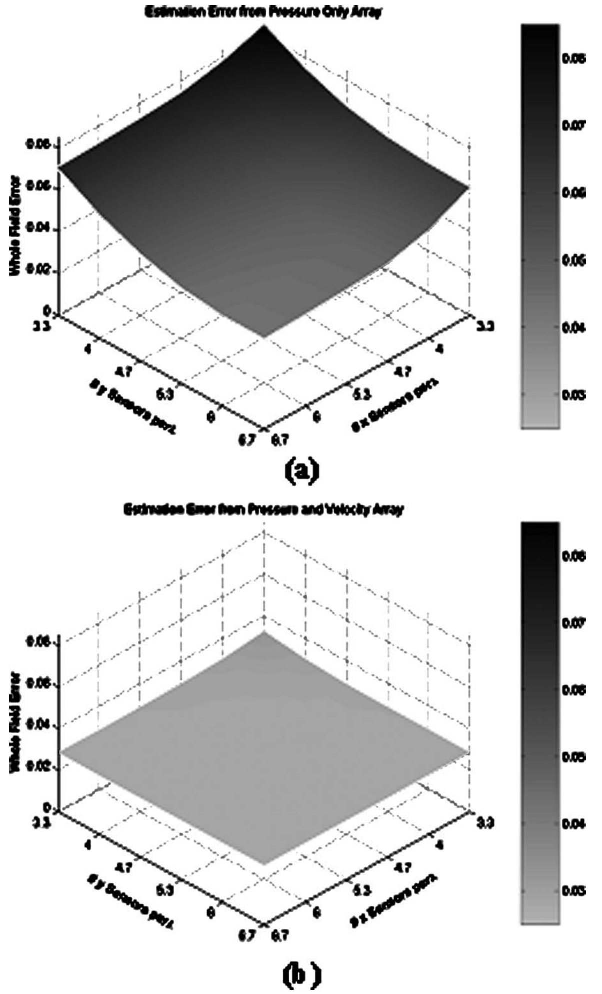

FIG. 6. (a) The estimation error for NAH reconstructions from pressure measurements as a function of sensors per spatial wavelength. (b) Estimation error for NAH reconstructions using preprocessed pressure and velocity measurements as a function of sensors per spatial wavelength.

C. Results

The results to follow correspond to the synthetic field generated by a 30.5 cm × 45.7 cm × 0.3175 cm plate vibrating in the 3,3 mode (1090 Hz), as shown in Fig. 4. These dimensions are chosen to match the dimensions used for the experimental validation presented in Sec. IV. The measurement plane is set to 5 cm and the estimation plane to 2 cm above the plate. Figures 6(a) and 6(b) show the resulting normalized whole field NAH estimation error plots for array sizes ranging from 10×10 to 20×20 for conventional pressure measurements and the processed pressure and velocity data. The data are presented as a function of the number of

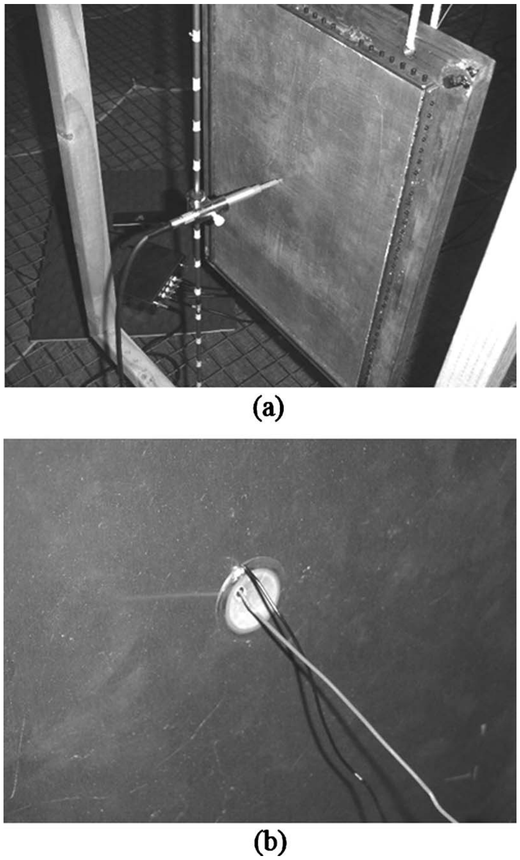

FIG. 7. (a) The experimental setup for the simply supported plate. (b) The piezoelectric patch used to excite the plate at its center.

sensors per spatial wavelength λ. This provides the reader with a qualitative sense of the relationship between estimation error and the sensor spacing.

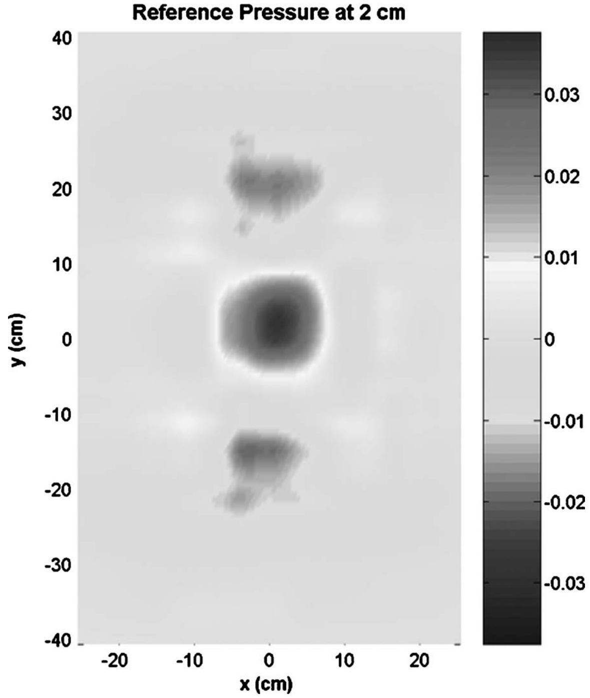

FIG. 8. The reference pressure at the 2 cm estimation plane against which the NAH reconstructions are compared.

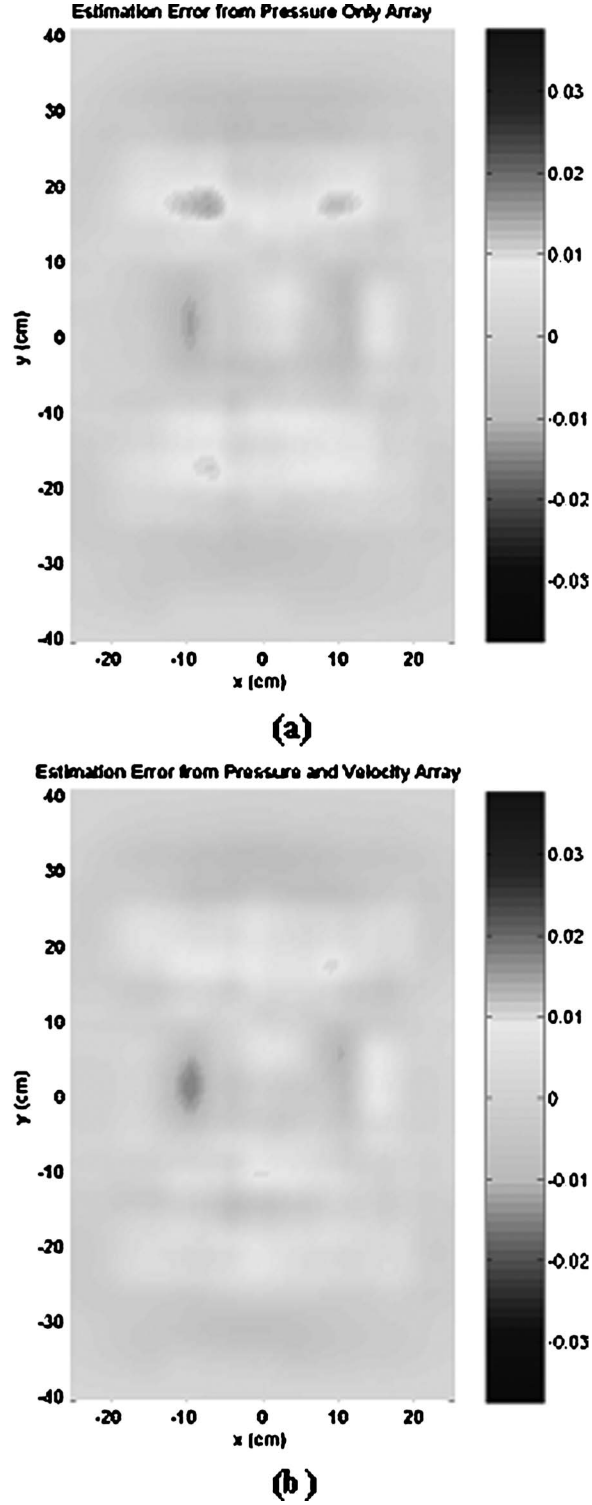

FIG. 9. (a) The pressure field reconstruction error at the 2 cm estimation plane from an 11×17 array of pressure measurements at 5 cm. (b) The pressure field reconstruction error at 2 cm from a 6×9 array of preprocessed pressure and in-plane velocity measurements at 5 cm.

These plots indicate that the inclusion of velocity field information at the hologram surface significantly improves the ability to reconstruct the field accurately. In fact, the NAH reconstruction using a 10×10 array of processed pressure and velocity measurements has a whole field error of 0.0326, which is slightly lower than the 0.0433 error for a 20×20 array of pressure measurements. These results show that the number of measurement locations can be reduced by

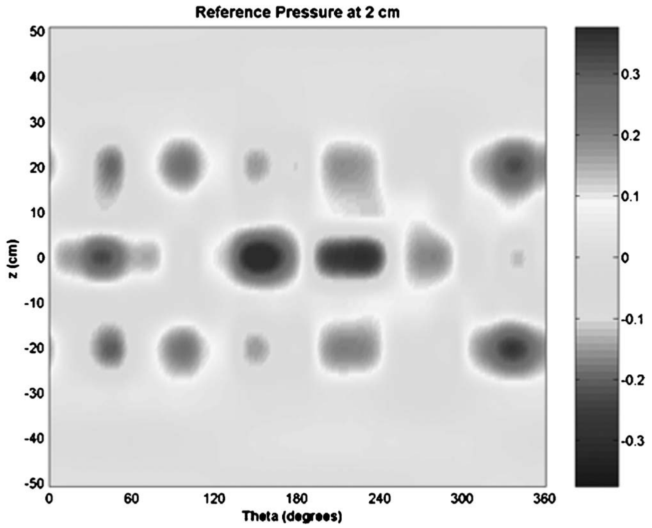

FIG. 10. The reference pressure field at 2 cm for the cylindrical test case.

about 75% when sensing equipment that measures pressure and velocity is used. This reduction seems reasonable since twice the information is being used in each direction. If a three channel probe is used to measure the field, a channel count reduction of 25% would also be realized for nonscanning systems. These results represent the theoretical optimal performance of the measurement schemes because the measurements have zero positioning, amplitude, and phase error.

IV. EXPERIMENTAL VALIDATION

A. Planar test case

An experimental setup is designed to approximate the simply supported plate used in the analytical investigation. Figure 7(a) shows the 30.5 cm × 45.7 cm × 0.3175 cm aluminum plate. It is attached along its edges to a heavy steel frame using cone point set screws to approximate the simply supported boundary condition. A 20-mm-diam piezoelectric patch, shown in Fig. 7(b), is used to excite the plate at its center. The plate and a measurement grid are suspended in an anechoic chamber for data acquisition. A single Microflown ultimate sound probe (USP) is used to scan the field to obtain the pressure and in-plane velocities required for the modified bicubic Hermite interpolation method. The plate is excited at 1090 Hz corresponding to the 3,3 operating shape. The field is sampled at 2 and 5 cm from the plate as in the analytical case. The vertical and horizontal step distance is set to 5 cm and the plate is overscanned in both directions yielding a 50 cm × 80 cm overall measurement array size. The 2 cm measurement again serves as the reference against which the NAH reconstructions are compared.

Figure 8 shows the reference pressure as measured on the 2 cm estimation plane. An 11 × 17 array of pressure measurements at 5 cm is used to reconstruct the pressure at the estimation plane using the traditional Fourier NAH method. The pressure only reconstruction is then compared to the reconstruction using a 6 × 9 array of pressure and velocity measurements spanning the same area. Figures 9(a) and 9(b) show the reconstruction error obtained by differencing the reference pressure and the reconstructions.

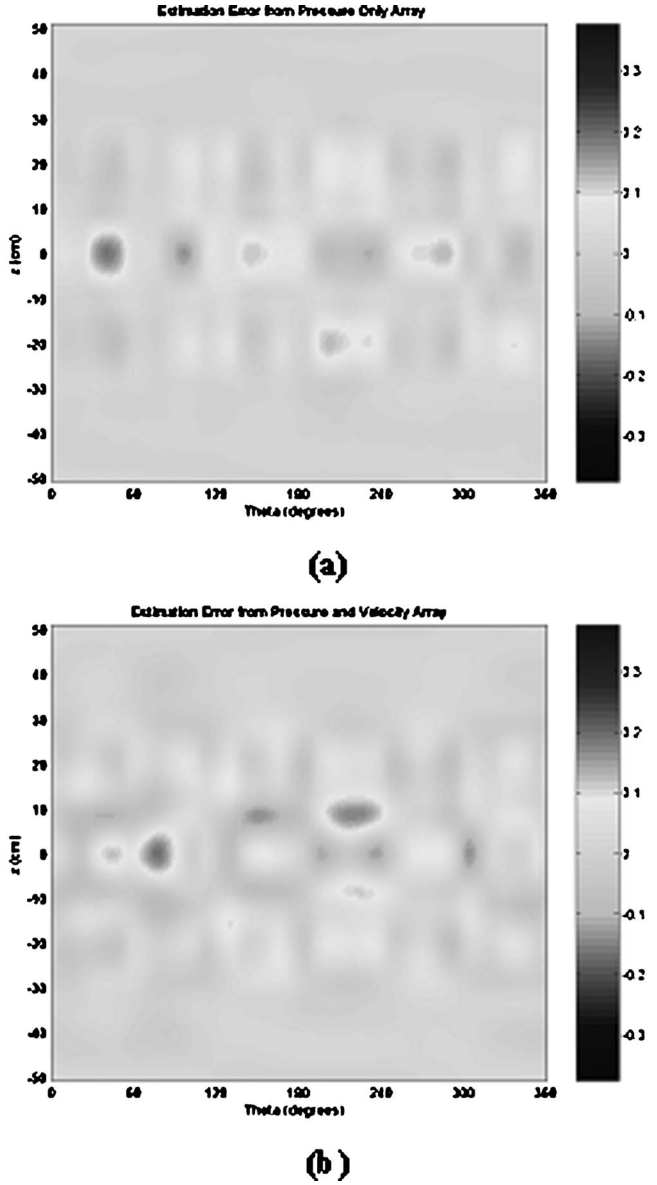

FIG. 11. (a) The pressure field reconstruction error at the 2 cm estimation plane from an 11 × 14 array of pressure measurements at 4 cm. (b) The pressure field reconstruction error at 2 cm from a 7 × 7 array of preprocessed pressure and in-plane velocity measurements at 4 cm.

Both NAH reconstructions are able to accurately characterize the pressure field on the estimation plane. The normalized whole field estimation error for the NAH reconstruction using only pressure measurements is 0.051, while the error for the reconstruction using the processed pressure and velocity data is 0.039. The reconstruction using the processed data is slightly more accurate than the conventional reconstruction with 70% fewer measurements. This corresponds well with the simulated results.

B. Cylindrical test case

A cylindrical ABS plastic tube is used for this test case. The tube dimensions are: 10.2 cm inner diameter, 10.8 cm outer diameter, 50.8 cm length. Simply supported boundary conditions are approximated at the tube ends using tapered conical plugs. The tube is driven at 1524 Hz with the same

20 mm piezoelectric patch used for the plate. This excitation corresponds to the 3,3 operating shape. Scans are made at 2 and 4 cm radial distances from the outer surface of the tube. Figure 10 shows the reference field at 2 cm. The resulting reconstruction error from an 11×14 array of pressure measurements at 4 cm is presented in Fig. 11(a). The vertical step distance is 10.2 cm and the incremental rotation angle is 27.7°. The reconstruction error shown in Fig. 11(b) is obtained using a 7×7 array of pressure and velocity measurements.

Both reconstructions retain the correct modal shape. However, the reconstruction utilizing the processed pressure and velocity measurements is more accurate at the peak amplitudes. The normalized whole field error for the conventional NAH reconstruction is 0.030. The error for the reconstruction based on pressure and velocity measurements is 0.024. Once again the NAH reconstruction using the proposed preprocessing method is able to provide slightly better reconstruction with 70% fewer measurements locations.

V. CONCLUSIONS

Based on the analytical and experimental results presented in this work, a 70% reduction in the number of measurement locations required for NAH is possible when pressure and in-plane velocities are used. For cases where subarrays of sensors are required to scan the field, the proposed preprocessing method reduces significantly the amount of repositioning, and therefore time, required. The subarrays could also be increased in size up to three and a half times if the same number of sensors is used. It should also be noted that the proposed interpolation method is applicable to other reconstruction methods, such as IBEM, that rely on a spatial sampling of the pressure field.

ACKNOWLEDGMENTS

The authors would like to thank Microflown Technologies for the use of the USP sensor. This work was supported by NASA and the National Science Foundation.

[1] E. G. Williams and J. D. Maynard, "Holographic imaging without the wavelength resolution limit," Phys. Rev. Lett. **45**, 554–557 (1980).

[2] J. D. Maynard, E. G. Williams, and Y. Lee, "Near-field acoustic holography. I. Theory of generalized holography and the development of NAH," J. Acoust. Soc. Am. **78**, 1395–1413 (1985).

[3] E. G. Williams, *Fourier Acoustics: Sound Radiation and Nearfield Acoustical Holography* (Academic, London, 1999).

[4] E. G. Williams, H. D. Dardy, and K. B. Washburn, "Generalized nearfield acoustical holography for cylindrical geometry: Theory and experiment," J. Acoust. Soc. Am. **81**, 389–407 (1987).

[5] T. Antoine, J. Catalfaud, and C. Aujard, "Meeting noise regulations with nearfield acoustic holography," Sound and Vibration Magazine, 18–20, May 2003.

[6] D. Vaucher de la Croix, P. Chevret, and F. Perrin, "Use of acoustical holography in 3D interiors measurements," in *Proceedings of International Congress and Exposition on Noise Control Engineering, Dearborn, MI, August 2002*.

[7] W. A. Veronesi and J. D. Maynard, "Digital holographic reconstruction of sources with arbitrarily shaped surfaces," J. Acoust. Soc. Am. **85**, 588–598 (1989).

[8] G.-T. Kim and B.-H. Lee, "3-D sound source reconstruction and field reprediction using the helmholtz integral equation," J. Sound Vib. **136**, 245–261 (1990).

[9] Z. Wang and S. F. Wu, "Helmholtz equation-least squares method for reconstructing the acoustic pressure field," J. Acoust. Soc. Am. **102**, 2020–2032 (1997).

[10] N. Rayess and S. F. Wu, "Experimental validations of the HELS method for reconstructing acoustic radiation from a complex vibrating structure," J. Acoust. Soc. Am. **107**, 2955–2964 (2000).

[11] T. Loyau, J. Pascal, and P. Gaillard, "Broadband acoustic holography reconstruction from acoustic intensity measurements. I. Principle of the method," J. Acoust. Soc. Am. **84**, 1744–1750 (1988).

[12] R. Visser, "Inverse source identification based on acoustic particle velocity measurements," in *Proceedings of the International Congress and Exposition on Noise Control Engineering*, INTERNOISE 2002, Dearborn, MI, August 2002.

[13] H. E. de Bree, "The Microflown: An acoustic particle velocity sensor," Acoust. Aust. **31**, 91–94 (2003).

[14] F. Jacobsen and H. E. de Bree, "A comparison of P-P and P-U sound intensity measurement systems," in *Proceedings of the Eleventh International Congress on Sound and Vibration*, St. Petersburg, Russia, July 2004, pp. 3159–3166.

[15] L. Locey, "Analysis and comparison of three acoustic energy density probes," Masters of Science Degree thesis, Brigham Young University, December 2004.

[16] M. Mortenson, *Geometric Modeling Second Edition* (Wiley, New York, 1997).

[17] G. Farin, *Curves and Surfaces for Computer-Aided Geometric Design* (Academic, New York, 1993).